

Receptive field asymmetries produce color-dependent direction selectivity in primate lateral geniculate nucleus

Save Sight Institute and ARC Centre of Excellence in Vision Science, University of Sydney, Australia, & Department of Optometry and Vision Sciences, University of Melbourne, Australia

Chris Tailby



William J. Dobbie

Discipline of Physiology, University of Sydney, Australia



Samuel G. Solomon

Discipline of Physiology and ARC Centre of Excellence in Vision Science, University of Sydney, Australia



Brett A. Szmajda

Department of Optometry and Vision Sciences, University of Melbourne, Australia



Maziar Hashemi-Nezhad

Discipline of Anatomy and Histology, University of Sydney, Australia



Jason D. Forte

Department of Psychology, University of Melbourne, Australia



Paul R. Martin

Save Sight Institute and ARC Centre of Excellence in Vision Science, University of Sydney, Australia



Blue-on receptive fields recorded in primate retina and lateral geniculate nucleus are customarily described as showing overlapping blue-on and yellow-off receptive field components. However, the retinal pathways feeding the blue-on and yellow-off subfields arise from spatially discrete receptor populations, and recent studies have given contradictory accounts of receptive field structure of blue-on cells. Here we analyzed responses of blue-on cells to drifting gratings, in single-cell extracellular recordings from the dorsal lateral geniculate nucleus in marmosets. We show that most blue-on cells exhibit selectivity for the drift direction of achromatic gratings. The standard concentric difference-of-Gaussians (DOG) model thus cannot account for responses of these cells. We apply a simple, anatomically plausible, extension of the DOG model. The model incorporates temporally offset elliptical two-dimensional Gaussian subfields. The model can predict color-contingent direction and spatial tuning. Because direction tuning in blue-on cells depends on stimulus chromaticity, spatial frequency, and temporal frequency, this property is of little value as a general mechanism for image movement detection. It is possible that anatomical wiring for color selectivity has constrained the capacity of blue-on cells to contribute to spatial and motion vision.

Keywords: blue-on, koniocellular, direction selective, lateral geniculate nucleus, marmoset

Citation: Tailby, C., Dobbie, W. J., Solomon, S. G., Szmajda, B. A., Hashemi-Nezhad, M., Forte, J. D., & Martin, P. R. (2010). Receptive field asymmetries produce color-dependent direction selectivity in primate lateral geniculate nucleus. *Journal of Vision*, 10(8):1, 1–18, <http://www.journalofvision.org/content/10/8/1>, doi:10.1167/10.8.1.

Introduction

The present study concerns an unusual property of neurons that support the blue–yellow axis of color vision. Early investigations identified “blue-on” receptive fields in the retina and lateral geniculate nucleus of anesthetized monkeys (DeMonasterio & Gouras, 1975; DeValois, Abramov, & Jacobs, 1966; Dreher, Fukada, & Rodieck, 1976; Wiesel & Hubel, 1966). These receptive fields were described as showing large, spatially overlapping, blue-on

and yellow-off subfields, consistent with a specialization to carry color signals. More recent studies showed however that when stimulated with achromatic drifting gratings, many blue-on cells show selectivity for grating drift direction (Forte, Hashemi-Nezhad, Dobbie, Dreher, & Martin, 2005; Tailby, Solomon, & Lennie, 2008; Tailby, Szmajda, Buzás, Lee, & Martin, 2008). Here we present a model to account for this property.

Color selectivity in blue-on cells is attributable to On-type input originating in short-wavelength-sensitive (S or “blue”) cones and Off-type input originating in medium-

and long-wavelength-sensitive (ML or “red and green”) cone photoreceptors (Derrington, Krauskopf, & Lennie, 1984; Lee, Valberg, Tigwell, & Tryti, 1987). Combined in vivo recording and cell labeling demonstrated that blue-on ganglion cells in macaque retina, the presumptive inputs to blue-on LGN neurons (Szmajda, Martin, & Grünert, 2008), show distinct “small field bistratified” (SBS) morphology with dendritic arbors in both the inner (On) and the outer (Off) subdivisions of the inner plexiform layer (Crook et al., 2009; Dacey & Lee, 1994). The inner dendritic tier of SBS cells contacts the axon terminals of bipolar cells selective for S cones (Calkins, Tsukamoto, & Sterling, 1998; Ghosh & Grünert, 1999; Ghosh, Martin, & Grünert, 1997; Marshak, Stafford, Jacoby, & Kouyama, 1995). A sparse outer tier stratifies in the Off subdivision of the inner plexiform layer. Here, yellow-off excitation could be delivered by bipolar cells selective for ML cones (Calkins et al., 1998; Ghosh & Grünert, 1999; Percival, Jusuf, Martin, & Grünert, 2009).

The studies cited above chiefly focused on how bistratified morphology determines chromatic selectivity of SBS cells. How bistratified morphology could influence responses of blue-on cells to achromatic stimuli remains however largely unexplored. The inner and outer dendritic tiers of SBS cells can differ substantially in both shape and spatial position (Dacey, 1993; Dacey & Lee, 1994; Percival et al., 2009; Silveira et al., 1999; Yamada, Silveira, Gomes & Lee, 1996). Accordingly, studies in macaque retina demonstrated that the S-cone-driven and the ML-cone-driven receptive fields’ subfields of blue-on cells can be non-circular, non-concentric, and have different response latencies (Chichilnisky & Baylor, 1999; Field et al., 2007). This calls into question the validity of simple difference-of-Gaussians models to account for spatial properties of these cells.

Here, we explore the potential contribution of dendritic field asymmetries to color-contingent direction selectivity. We address the basis of this property by first measuring the size and shape of dendritic tiers of SBS cells in marmoset retinas. These anatomical data are taken as constraints on synthetic linear receptive fields. The simulations predict that dendritic field asymmetries of SBS cells, when coupled with phase lags between S and ML cone inputs, can yield direction selectivity for achromatic gratings. We show that the model can account for responses of blue-on cells recorded in marmoset lateral geniculate nucleus.

Methods

Data set

Single-cell responses were reanalyzed from our previous studies, where details of animal preparation and recording techniques are given (Blessing, Solomon, Hashemi-Nezhad,

Morris, & Martin, 2004; Tailby, Szmajda et al., 2008; Victor, Blessing, Forte, Buzás, & Martin, 2007). Cells were encountered in extracellular single-unit recordings from the lateral geniculate nucleus of common marmoset monkeys (*Callithrix jacchus*). The primary data set comprised responses of 73 blue-on cells recorded from a total of 27 marmosets (14 females). Thirteen of the female animals showed trichromatic color vision phenotype (as evidenced by the presence of red–green opponent responses in parvocellular geniculate cells). The other female marmoset, and all male marmosets, showed dichromatic color vision phenotype consistent with the presence of SWS cones and a single cone type in the medium- to long (ML)-wavelength-sensitive range. No systematic differences in responses of blue-on cells to achromatic or SWS-cone-selective stimuli were seen on comparing dichromatic and trichromatic marmosets, so data were pooled for analysis. For purposes of comparison, responses of parvocellular ($n = 417$) and magnocellular neurons ($n = 80$) extracted from a database of responses from 40 marmosets were reanalyzed. Cells were identified as belonging to parvocellular, magnocellular, or blue-on response class using a battery of tests including measurement of spatial frequency response, temporal frequency response, and contrast response functions. The classification was confirmed by histological reconstruction for 244/568 cells (42%). Of the blue-on cells that were reconstructed and could be assigned unambiguously to one LGN layer, the great majority (22/29, 76%) was located in layer K3 between the parvocellular and magnocellular layers. The remaining seven cells were located in the parvocellular layers. No systematic differences were seen between blue-on receptive fields encountered in koniocellular and parvocellular layers, so results were pooled for analysis.

Visual stimuli

Visual stimuli were drifting sine gratings. Each visually responsive cell was initially classified using manually controlled stimuli and its receptive field mapped on a tangent screen. In early experiments, stimuli were generated using a VSG Series Three video signal generator (Cambridge Research Systems, Cambridge, UK) and presented on a Reference Calibrator Plus monitor (Barco) at a frame refresh rate of 80 Hz. In later experiments, visual stimuli were generated using Open GL commands controlled via freely available software (Expo, Peter Lennie) and presented on a Sony G520 monitor refreshed at 120 Hz. Monitors were linearized and colorimetrically calibrated as described below; mean luminance was 20–60 Cd/m². Stimuli were viewed from a distance of 114 cm via a front-silvered mirror mounted on a gimballed stand interposed in the optical path. Action potentials arising from visually responsive cells were identified and time-stamped to an accuracy of 0.1 ms. Cumulatively, 5–10 s of

activity was recorded for each stimulus condition. The amplitude and phase of the Fourier component at the frequency of stimulation was extracted from peristimulus time histograms.

The driving voltage to the red, green, and blue guns of the stimulus monitor was adjusted to produce either equal-energy achromatic or cone-selective (“silent substitution”) gratings, using knowledge of the spectral radiance distribution of the monitor phosphors, the peak sensitivity of marmoset cone photoreceptors, and the spectral absorption characteristics of the optic media and macular pigment (Blessing et al., 2004; Brainard, 1996; Tailby, Szmajda et al., 2008). The S-cone-selective stimulus produced 60–80% contrast in S cones and less than 5% contrast in ML class cones. The ML-cone-selective (“silent S”) stimulus produced over 60% contrast in ML class cones and less than 5% contrast in S cones.

Analysis of direction bias

Direction tuning was calculated from responses to a set of 12 or 16 drifting gratings (the orientation varied in steps of 30 or 22.5 deg). The direction-selectivity index (DI) was determined from these response measurements as the circular variance (Levick & Thibos, 1982):

$$DI = \frac{\left| \sum_{\theta=0}^{2\pi} R_{\theta} e^{i\theta} \right|}{\sum_{\theta=0}^{2\pi} R_{\theta}}, \quad (1)$$

where DI is the direction index, R_{θ} is the response of the neuron to a stimulus with orientation θ between 0 and 2π radians, and i is the imaginary unit $\sqrt{-1}$. A DI value of 1 indicates response to only one direction of motion and a DI value of 0 indicates the same response to all directions.

Modified difference-of-Gaussians model

The standard difference-of-Gaussians (DoG) model presented by Enroth-Cugell and Robson (1966) and Rodieck & Stone (1965) is spatially symmetric and spatiotemporally separable. Response amplitude in the spatial frequency domain is calculated as

$$R = C((K_c \pi r_c^2 e^{-(\pi r_c f)^2}) - (K_s \pi r_s^2 e^{-(\pi r_s f)^2})), \quad (2)$$

where R is the response amplitude (imp s⁻¹), C is the Michelson contrast of the stimulus, and f is the spatial frequency of the stimulus (Enroth-Cugell & Robson, 1966). The free parameters K_c , K_s , r_c , and r_s represent center peak sensitivity, surround peak sensitivity, center Gaussian radius, and surround Gaussian radius, respectively. Here,

we use a modified form of the DoG model, based on the two-dimensional Gaussian subfield model presented by Soodak (1986). In this modified DoG model, the center and surround subfields are specified as two-dimensional elliptical Gaussians that can have center positions, orientations, and latencies that differ from one another. The response amplitude of subfield n is given by

$$|r(f, \theta)| = \pi K_n w_{n1} w_{n2} \exp\left\{-\left(\pi w_{n1} w_{n2} f\right)^2 \left[\sin^2(\theta - \theta_n)/w_{n1}^2 + \cos^2(\theta - \theta_n)/w_{n2}^2\right]\right\}, \quad (3)$$

where K_n , w_{n1} , w_{n2} , and θ_n are the peak sensitivity (defined as positive for On subfields and negative for Off subfields), the width of the major axis, the width of the minor axis, and the orientation of the major axis of subfield n , respectively.

The response phase of subfield n is given by

$$\arg r(f, \theta) = 2\pi(X_{n0}^2 + Y_{n0}^2)^{0.5} \times \cos[\theta - \tan^{-1}(Y_{n0}/X_{n0})] + \phi_{n0}, \quad (4)$$

where X_{n0} , Y_{n0} , and ϕ_{n0} are the X coordinate of the center of subfield n , the Y coordinate of the center of subfield n , and the temporal phase delay of subfield n , respectively. The total response, represented as a complex number, is given by the sum of all of the subfield responses, i.e.,

$$R(f, \theta) = \sum_{n=1}^N |r_n(f, \theta)| \exp(i \arg r_n(f, \theta)), \quad (5)$$

where n indexes the individual subfield responses and N is the number of subfields. We fit the model to the amplitude of the response of marmoset LGN neurons using non-linear least square minimization (optimization toolbox, Mathworks, Natick, MA). Where multiple stimulus conditions were fit simultaneously, response amplitudes were normalized by stimulus contrast.

Morphology of blue-on retinal ganglion cells

The anatomical bias in SBS ganglion cells was estimated from cells labeled using intracellular injection or photo-filling in an in vitro whole-mount preparation. The methods for labeling ganglion cells are described fully in previously published studies, where other morphological parameters of these cells are described (Ghosh et al., 1997; Szmajda et al., 2008). For the present purposes, dendritic field size and orientation of labeled cells were analyzed from a Z-stack of digital images at 0.3–0.5 μm image spacing, acquired using a Zeiss AxioCam HRc color digital camera (Karl Zeiss, Oberkochen, Germany). Custom software written in

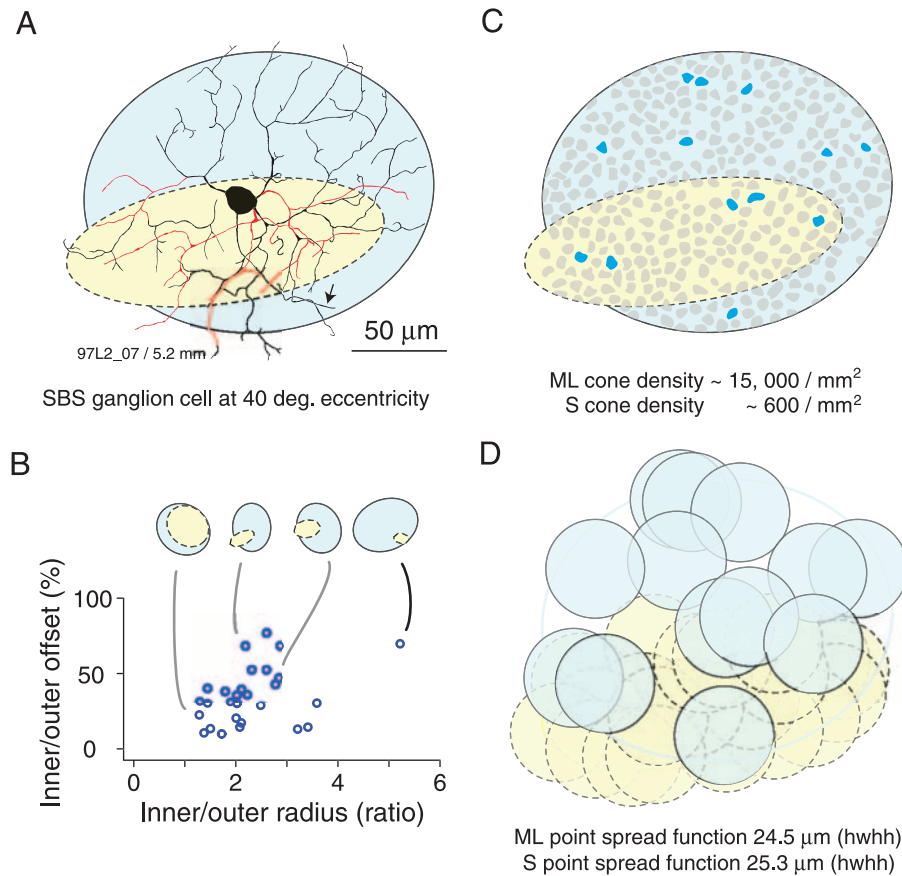


Figure 1. Spatial anisotropies in the dendritic field arrangement of small bistratified (SBS) cells. (A) *Camera lucida* drawing of the inner (black) and outer (red) dendritic tiers of a retrogradely labeled, photofilled SBS cell in marmoset retina (located at 5.2-mm eccentricity). Overlays show best fitting ellipses to the inner tier (blue, solid outline) and outer tier (yellow, dashed outline). (B) Scatter plot showing spatial offset of the inner ellipse relative to the outer ellipse (y -axis) and the ratio of circle equivalent radii of the inner and outer ellipses (x -axis) for 28 SBS cells. Insets show spatial layout of the inner (blue, solid outline) and outer (yellow, dashed outline) ellipses for sample cells. (C) Best fitting ellipses from (A) superimposed on a sample of cone mosaic from peripheral marmoset retina; 13 of the 318 cones within the ellipses have been randomly assigned as S cones (blue puncta), and the remaining cones are assigned as ML cones (gray puncta). (D) Influence of optical aberrations on the spatial receptive field of the cell shown in (C). The inner tier is assumed driven exclusively by S cones that fall within the blue ellipse in (C); the outer tier exclusively by ML cones that fall within the yellow ellipse in (C). Optical imperfection-induced smear in the spatial sampling of each individual cone contributing to the SBS receptive field is indicated by the colored areas (blue, solid outlines: S cones; yellow, dashed outlines: ML cone). See text for details of optical calculations.

MATLAB (Image processing toolbox, Mathworks, Natick, MA) was used to analyze each stack of images. Dendritic field dimensions were measured by tracing a polygon around the outermost tips of the dendrites forming the inner and outer strata. The shape and position of each stratum were parameterized by the radius and position of the area equivalent ellipse calculated from the polygon.

Results

We first present a morphological analysis of the dendritic arbor patterns of small bistratified (SBS) cells. We use these data to generate synthetic receptive fields, from which we calculate responses to drifting achromatic and cone-

selective gratings. We show how anatomical asymmetry can produce selectivity for image motion. We then present data recorded from blue-on cells in marmoset LGN, the central targets of SBS cell axons (Szmajda et al., 2008), and show that the functional properties of these cells are compatible with spatial and temporal asymmetries of On and Off subfields. These asymmetries may arise in the dendritic fields of SBS cells.

Spatial asymmetry of inputs to small bistratified cells

Figure 1A shows a drawing of an SBS cell in marmoset retina labeled by photofilling. As previously shown for human, macaque monkey, Cebus monkey, and marmoset

retina (Dacey, 1993; Ghosh et al., 1997; Rodieck & Watanabe, 1993; Silveira et al., 1999; Szmajda et al., 2008), the outer dendritic tier (drawn here in red) and the inner dendritic tier (drawn here in black) show distinct organization. The inner tier is larger than the outer tier, and the two tiers differ in their axis of elongation. We fit separate ellipses to the inner and outer tiers, shown by the superimposed shaded regions in Figure 1A (see Methods section). Measurements were made for a sample of SBS cells at eccentricities ranging from 2.9 degrees to 78.4 degrees (mean = 22.3°, $SD = 15^\circ$). For all cells, the inner tier is larger than the outer tier (geometric mean ratio of equivalent circle radius = 2.19, $SD = 0.84$, $n = 28$). Furthermore, the two tiers are not concentric (Figure 1B). We observed no consistent trend in the displacement of the inner and outer tiers with respect to major retinal landmarks (fovea, vertical and horizontal meridians, optic disc); the offset is distributed in an apparently random manner (mean offset 35.4% of inner diameter radius, $SD = 19.2$, $n = 28$). These data indicate that the two dendritic tiers sample from at least partially distinct non-concentric regions of visual space.

It could be argued that optical imperfections of the eye would obliterate the effect of anatomical asymmetries in SBS cells. Figure 1C illustrates why this is unlikely to be the case. This panel shows (at the same scale as Figure 1A) a sample of cone mosaic in peripheral marmoset retina (data from the study by Percival et al., 2009) vignetted by the dendritic field outlines from Figure 1A. At this eccentricity in marmoset retina, S cones are distributed randomly and make up 3–5% of all cones (Martin & Grünert, 1999; Martin, Grünert, Chan, & Bumsted, 2000); therefore 13 of the 318 cones (4.1%) in the field have been randomly assigned as S cones. The effect of the eye's optical aberrations is illustrated in Figure 1D. Here the positions of cones are marked by circles with the same radius as the root mean square of the point spread function at 40 degrees eccentricity in the marmoset eye. Values were calculated from published data for marmoset eye (Troilo, Howland, & Judge, 1993) using ray-tracing software (ZEMAX, Bellevue, WA). For simplicity, higher order aberrations (cf., for example, Williams & Hofer, 2003) are not considered. Values for ML cones were calculated for 555 nm and values for S cones were calculated for 420 nm; all calculations were referenced to an in-focus 555-nm image plane at the fovea. At this eccentricity, optical imperfections have comparable effects on S and ML cones, so the relative positions and scales of the S and ML fields are effectively preserved. It may seem surprising that quite similar point spread functions are predicted for S cones (25.3 μm half-width at half-height) and ML cones (24.5 μm half-width at half-height). The explanation is that longer wavelengths become defocused more than shorter wavelengths with increasing distance from the fovea: parallel calculations for the fovea predict 15.5 μm half-width at half-height for S cones and 6.5 μm half-width at half-height for ML cones.

In the following, we elaborate the standard DOG model to incorporate spatial and chromatic asymmetries. We explore the potential of such asymmetries to influence the functional properties of blue-on cells. Because we did not have a priori knowledge of the position of individual S and ML cones within the receptive field of the SBS cells we measured, we did not use detailed optical calculations to analyze the effects of blur on a cell-by-cell basis. The important point here is that the point spread functions (under the degraded optical conditions prevailing in peripheral retina) are rather similar for S and ML cones, yet the optics are nevertheless good enough to preserve some spatial structure in signals transmitted from the cone mosaic.

Direction selectivity in simulated small bistratified cell receptive fields

On the basis of the anatomical data shown in Figure 1B, we simulated receptive fields for each of our anatomically reconstructed SBS cells using the modified DOG model described in Equations 3–5 (see Methods section). We defined the relative shapes and positions of On and Off subfields using ellipse parameters derived for the inner and outer tiers, respectively. For simplicity, we specified a constant 7-ms delay of the Off subfield relative to the On subfield (Crook et al., 2009). The integrated sensitivity (“volume”) of the On subfield was normally set to be 1.2 times the volume of the Off subfield (Tailby, Solomon et al., 2008; Tailby, Szmajda et al., 2008); simulations in which this parameter was modified are described in a later section. The response of the simulated receptive field is calculated as the sum of the signals (amplitude and phase) arising in the individual subfields (see Methods section).

The results of one such simulation, based on the morphology of the neuron shown in Figure 1A, are shown in Figure 2. Figure 2A shows the spatial layout of the receptive field together with the temporal kernels of the On and Off subfields. Figure 2B shows the simulated direction tuning curves for achromatic gratings drifting at 5 Hz. The simulation reveals spatial frequency-dependent orientation and direction biases. At low spatial frequency (0.04 cycles per degree [cyc/deg]) the tuning curve shows a weak direction bias, but as spatial frequency increases the response becomes more direction selective and shows substantial bias at a spatial frequency of 0.4 cyc/deg. As spatial frequency is further increased (4 cyc/deg), the response becomes much weaker and shows orientation selectivity, reflecting spatial anisotropy of the subfield with the highest spatial resolution (Chichilnisky & Baylor, 1999; Soodak, 1986).

Direction selectivity was quantified by calculating a direction index (DI, see Methods section), which takes values between 0 (equal responses to all directions) and 1 (responses exclusively to one direction). The sample receptive field has a DI of 0.27 for the 0.4 cyc/deg tuning curve shown in Figure 2B. The direction bias arises through

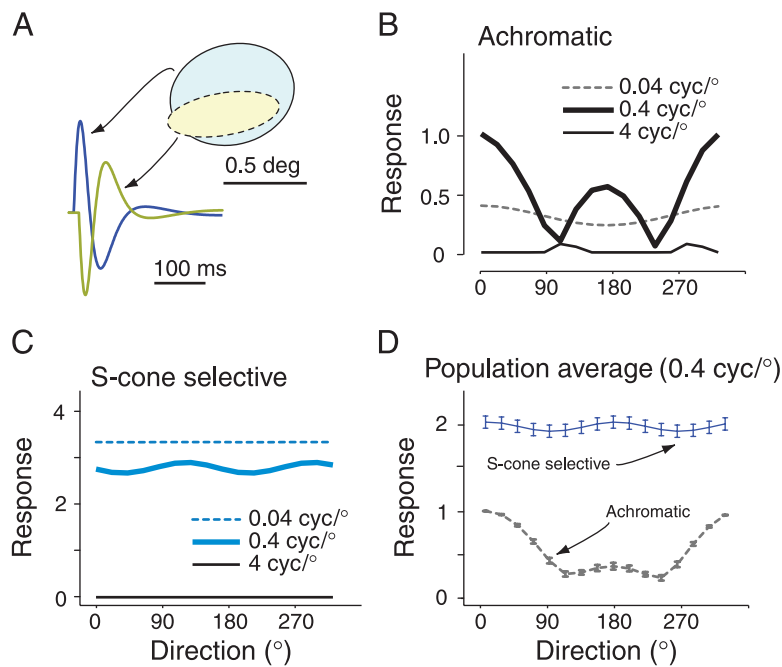


Figure 2. Direction tuning in simulated small bistratified (SBS) cells. (A) Spatial and temporal profiles of the receptive field. The spatial profile of the On (blue, solid outlines) and Off (yellow, dashed outlines) Gaussian subfields, drawn here as ellipses to a 2 standard deviation contour boundary, corresponds to that of the best fitting ellipses of the cell shown in Figure 1A. The On subfield draws input from S cones. The Off subfield draws input from ML cones. The temporal profile of each subfield is a biphasic function. The latency of the Off subfield is delayed 7 ms relative to that of the On subfield. (B) Direction tuning of this receptive field for achromatic gratings drifting at 4.4 Hz. Response amplitude is normalized to the best achromatic response. (C) Same as (B) but for S-cone-isolating gratings. (D) Population average direction tuning curves, calculated from simulations based on the 28 reconstructed SBS cells shown in Figure 1C, for achromatic (black) and S-cone-isolating (blue) 0.4 cyc/deg gratings drifting at 4.4 Hz. Error bars show standard errors of the mean. Direction tuning curves for each cell were aligned to the direction of maximal response, then normalized in amplitude relative to the best achromatic response.

the interaction between On and Off subfields. It disappears when only one of the subfields is modulated by the stimulus, as occurs when S-cone-selective gratings are used to stimulate the On subfield in isolation (Figure 2C). At low spatial and temporal frequencies, responses to achromatic gratings are weaker than responses to S-cone gratings because there is an antagonistic interaction between On and Off subfields. The degree of direction selectivity also depends on stimulus temporal frequency, as variation in temporal frequency will change the relative response phase of the On and Off subfields (not shown).

Figure 2D summarizes achromatic and S-cone-selective direction tuning for simulations using the anatomical parameters of each of the SBS cells shown in Figure 1B. Simulated responses to 0.4 cyc/deg, 4.4-Hz gratings are shown. The temporal frequency is the geometric mean frequency at which responses to achromatic gratings were measured in the physiological experiments, as described in the next section. Curves for each cell were aligned to the preferred achromatic direction, normalized to the best achromatic response, then averaged. The population average tuning curve shows pronounced direction bias (DI = 0.33), even in the face of the considerable morphological variation evident in Figure 1. As noted above, because the direction

selectivity emerges from antagonistic interaction between On and Off subfields, it is eliminated when the On subfield is stimulated alone (Figure 2D, solid blue curve). For the same reason, response amplitude is greater when the On subfield is stimulated alone.

The reader should note that the specifics of the tuning curves shown in Figure 2, including their associated DIs, will vary with the specific simulation parameters chosen: changes in the On/Off volume ratio and/or relatively latency will change the tuning curves. The measured direction selectivity also depends on cell-specific relationships between receptive field structure and the spatial and temporal frequencies of the stimulus. We return to this issue below; here we wish to emphasize the conceptual implication of the anatomical data, that is, spatial and temporal offsets between spectrally selective On and Off subfields can produce color-contingent direction biases.

Direction selectivity in recordings from blue-on cells in LGN

Convergent anatomical and physiological evidence shows that the small bistratified (SBS) ganglion cell class

is the source of retinal input to the majority of blue-on cells in the LGN (Dacey & Lee, 1994; Martin, White, Goodchild, Wilder, & Sefton, 1997; Roy et al., 2009; Szmajda et al., 2008; reviewed by Hendry & Reid, 2000). Blue-on cells are encountered principally in the koniocellular layers of the LGN, of which layer K3 is relatively broad (and hence easily targeted) in marmoset LGN. We thus targeted this layer for recording blue-on receptive fields. When a blue-on cell was encountered, we sought (by manually adjusting the direction, spatial frequency, and temporal frequency of a drifting achromatic grating) a combination of spatial and temporal frequencies that would evoke direction bias for achromatic gratings. We then measured direction tuning curves for gratings of spatial and temporal frequencies at and around these empirically identified values. Overt direction biases were only apparent in cells with strong S-cone input; they were not detected in PC or MC pathway cells.

Figures 3A–3F show responses of three blue-on cells. For each cell, response amplitude is plotted as a function of drift direction for achromatic (Figures 3A, 3C, and 3E) and S-cone-selective (Figures 3B, 3D, and 3F) gratings. The achromatic direction tuning curves for each cell (filled symbols, Figures 3A, 3C, and 3E) show direction biases, in that responses are strongly dependent on grating drift direction. The direction bias largely disappears when the cells are stimulated with S-cone-selective gratings (Figures 3B, 3D, and 3F). Direction selectivity indices (DI) for the cell shown in Figures 3A and 3B are 0.41 and 0.02, respectively; for the cell in Figures 3C and 3D, 0.27 and 0.04, respectively; for the cell in Figures 3E and 3F, 0.21 and 0.09, respectively. These data thus demonstrate direction biases in responses of blue-on cells to achromatic gratings, as predicted by the simulations shown in Figure 2.

For the cells shown in Figures 3C–3F, we also measured achromatic direction tuning at a non-optimal spatial frequency. These data are shown as the unfilled symbols in Figures 3C and 3E. For the cell in Figure 3C, increasing spatial frequency from 0.8 cyc/deg to 4.0 cyc/deg decreases the DI from 0.27 to 0.08. By contrast, for the cell in Figure 3E, increasing spatial frequency from 0.8 cyc/deg to 1.6 cyc/deg increases the DI from 0.05 to 0.21. We conclude that direction tuning biases in blue-on cells depend on the spatiotemporal frequency composition of the stimulus, consistent with the predictions illustrated in Figure 2.

Figures 3G–3J compare population average direction tuning curves for blue-on cells, parvocellular cells, and magnocellular cells. Data are normalized to maximum response amplitude but are otherwise shown in the same format as Figure 2D. For blue-on cells, achromatic gratings drifting in the preferred direction (Figure 3G) evoked, on average, more than double the response to gratings drifting in the opposite direction (mean ratio opposite/optimal = 0.42, $SD = 0.29$, $n = 69$; geometric mean spatial frequency = 1.08 cyc/deg, geometric mean temporal frequency = 4.4 cyc/s). For some blue-on cells, a spatiotemporal frequency

combination eliciting substantial direction selectivity could be found, whereas other cells showed only weak selectivity. Consistent with responses from individual cells, the population DI for S-cone-selective gratings (Figure 3H) is low (mean = 0.04, $SD = 0.03$, $n = 73$).

Average achromatic direction tuning data for 417 PC and 80 MC cells are shown in Figures 3I and 3J. As expected, PC cells and MC cells show mild orientation bias but negligible direction bias, consistent with a slightly elliptical receptive field (Forte et al., 2005; Passaglia, Troy, Rüttiger, & Lee, 2002; Smith, Chino, Ridder, Kitagawa, & Langston, 1990; White, Solomon, & Martin, 2001; Xu, Ichida, Shostak, Bonds, & Casagrande, 2002).

Distribution of population properties of blue-on cells is shown in Figures 3K–3M. The DI for achromatic and S-cone-selective gratings was not significantly correlated on a cell-by-cell basis (Figure 3K; correlation coefficient: 0.20, $r^2 = 0.04$, $p = 0.22$; regression analysis, $n = 40$). Within the resolution of our visual field mapping system, no clear trend was apparent for preferred direction for achromatic gratings referred to visual field angle (Figure 3L, $p = 0.56$, Rayleigh test of circular uniformity) or referred to a line joining the receptive field On-subfield center to the fovea (Figure 3M; $p = 0.97$, Rayleigh test of circular uniformity).

Of the blue-on cells that responded at greater than 10 spikes per second to drifting achromatic gratings, the majority (48/69, 70%) shows DI greater than 0.1. As a population, the DI of blue-on cells (geometric mean = 0.131) was significantly larger than that of PC cells (geometric mean DI = 0.029; Kruskal–Wallis test, $p < 0.01$) and MC cells (median DI = 0.026; Kruskal–Wallis test, $p < 0.01$). By contrast, DI for S-cone-selective gratings was greater than 0.1 in only 4% of cases (3/73; geometric mean DI = 0.033). In summary, blue-on cells in marmoset LGN show color- and spatial frequency-dependent selectivity for grating drift direction. Direction biases are not a feature of the direction tuning curves of PC and MC cells.

Applicability of a linear receptive field model of direction selectivity in blue-on cells

We next asked whether the linear receptive field model outlined in Equations 3–5 can capture the spatial tuning properties of the blue-on cells. For each blue-on cell, we simultaneously fit the model illustrated in Figure 2A to an achromatic direction tuning curve, an achromatic spatial frequency tuning curve, and an S-cone-selective spatial frequency tuning curve. All curves were obtained at the same temporal frequency. We forced the full model (consisting On and Off subfields) to capture the achromatic direction and spatial frequency tuning curves. We used the high-frequency limb of the S-cone-selective spatial frequency tuning curve to characterize the On subfield. This constraint was imposed in order to estimate the influence of the blue-on subfield in isolation, because many LGN

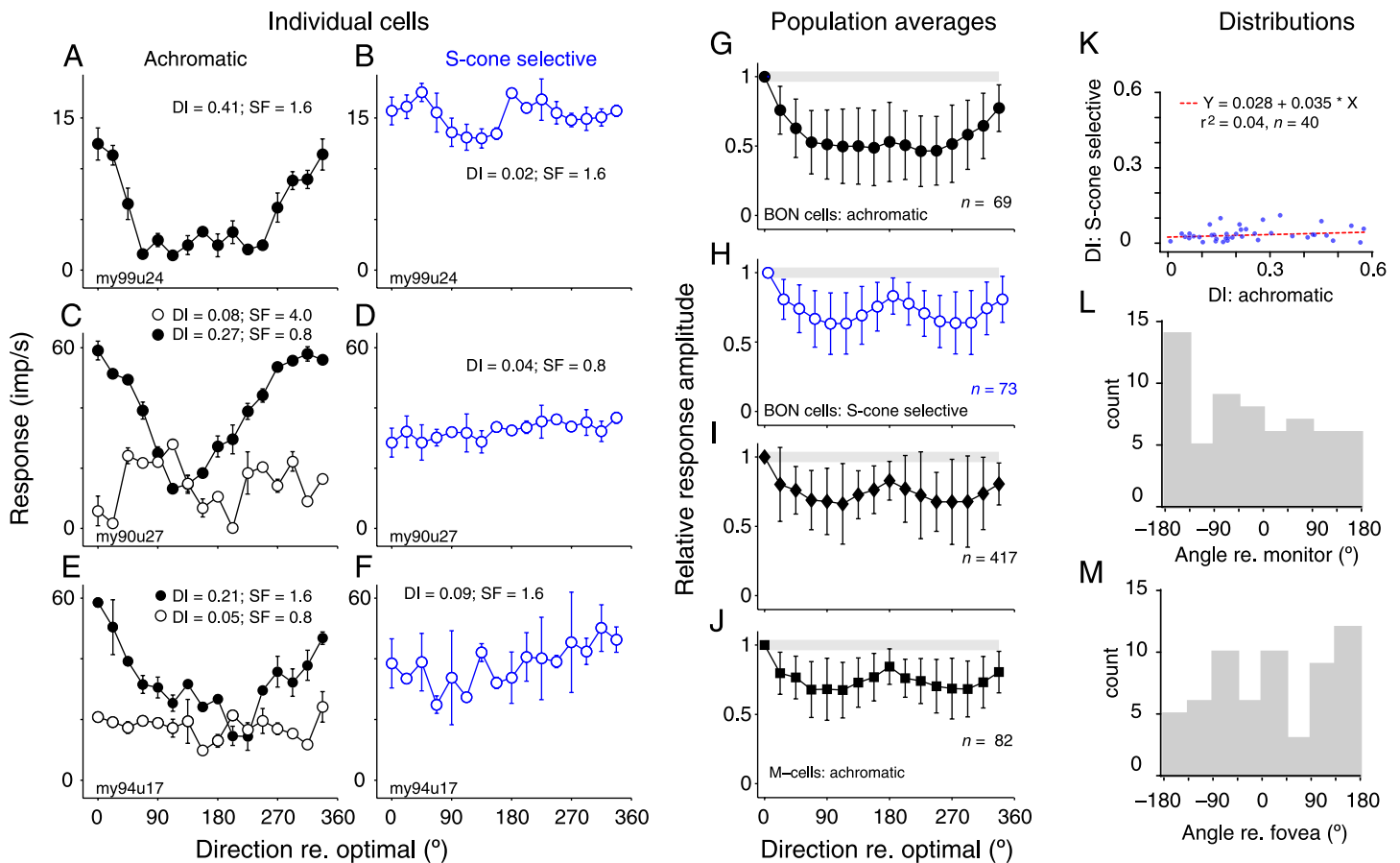


Figure 3. Direction tuning in blue-on cells recorded from marmoset LGN. Direction tuning of a sample blue-on cell for (A) drifting achromatic and (B) S-cone-isolating gratings (temporal frequency [TF] = 4 Hz). DI: direction index; SF: spatial frequency. Error bars show standard errors of the mean (in some cases smaller than the data symbol). Direction has been aligned to the drift direction of achromatic gratings evoking the largest response. (C) Achromatic and (D) S-cone-isolating direction tuning curves (TF = 4 Hz) for a second sample blue-on cell. Conventions as in (A) and (B). Open and closed symbols in (C) denote achromatic direction tuning functions measured, respectively, at preferred and non-preferred spatial frequencies. (E) Achromatic and (F) S-cone-isolating direction tuning curves (TF = 4 Hz) for a third sample blue-on cell. Conventions as in (A) and (B). (G) Population average achromatic direction tuning curve for 69 blue-on cells. Curves for each cell were aligned to the best direction, and response normalized to the best response, prior to averaging. Error bars show standard deviations. (H) Population average S-cone-isolating direction tuning curve for 73 blue-on cells. Curves were calculated, and conventions are the same as in (G). (I, J) Population average achromatic direction tuning curves for 417 PC cells and 82 MC cells. Curves were calculated, and conventions are the same as in G. (K) Scatter plot of DI measured with S-cone-isolating gratings against DI measured with achromatic gratings, showing the range of values obtained. Dashed line shows linear regression; r , residual sum of squares. (L) Histogram of preferred direction expressed relative the monitor (0 degrees indicates upward drift, 90 degrees indicates leftward drift). (M) Histogram of preferred direction expressed relative to the direction pointing from the receptive field to the fovea; r , Rayleigh coherence; p , probability, Rayleigh test of circular uniformity.

blue-on cells show response attenuation for low spatial frequency S-cone-selective gratings (Tailby, Solomon et al., 2008; Tailby, Szmajda et al., 2008; though see also Crook et al., 2009). As outlined above (see [Methods](#) section), we also constrained the Off subfield to have longer latency than the On subfield (Crook et al., 2009; Field et al., 2007; Tailby, Solomon et al., 2008).

Figures 4A–4F show model fits to data collected from 6 blue-on cells. Each row contains data from a single cell. Response amplitudes are normalized to 100% stimulus

contrast. The left column shows the direction tuning data, the center column shows the spatial frequency tuning data, and the right column shows a representation of the spatial receptive field derived from the model fit. The model is flexible enough to account for the variety of direction tuning curves observed in our sample. The quality of the fits (as indexed by the percentage of variance explained) decreases moving down the rows in the figure, from a maximum of 97% in Figure 4A to 81% in Figure 4F.

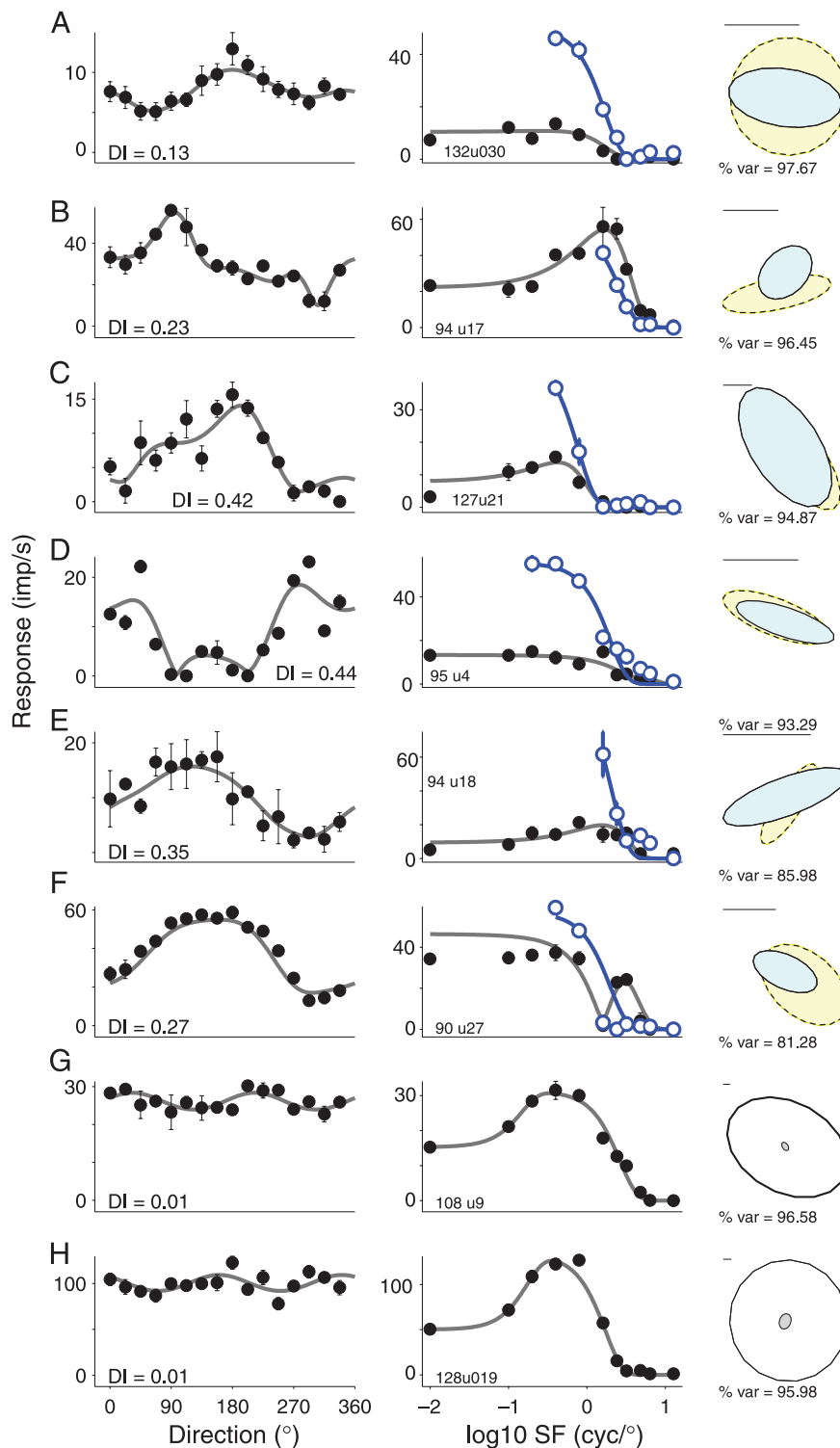


Figure 4. Fits of a linear receptive field model to direction and spatial frequency tuning data recorded from marmoset LGN neurons. Each row shows the raw responses (error bars show standard errors of the mean, in some cases smaller than the data symbol) and the fitted model (smooth lines) for an individual cell. (Left) Achromatic direction tuning curves. DI: direction index. (Center) Achromatic (filled black symbols) and S-cone-isolating (blue circles) spatial frequency tuning curves. Only the high-frequency limb of the S-cone-isolating spatial frequency tuning curve is shown. (Right) Representation of the spatial receptive field returned by the model fit. Dimensions of the 2-D Gaussians of the On (blue, solid outlines) and Off (yellow, dashed outlines) subfields of the model are drawn as ellipses of uniform sensitivity out to a two standard deviation contour boundary; % var: percentage of variance explained by the model fit. Scale bars correspond to 0.25°. (A–F) Six sample blue-on cells. (G) Sample PC cell. (H) Sample MC cell. Data for S-cone-isolating gratings are not shown in (G) and (H), and were not used in the model fits, as the cells were insensitive to them.

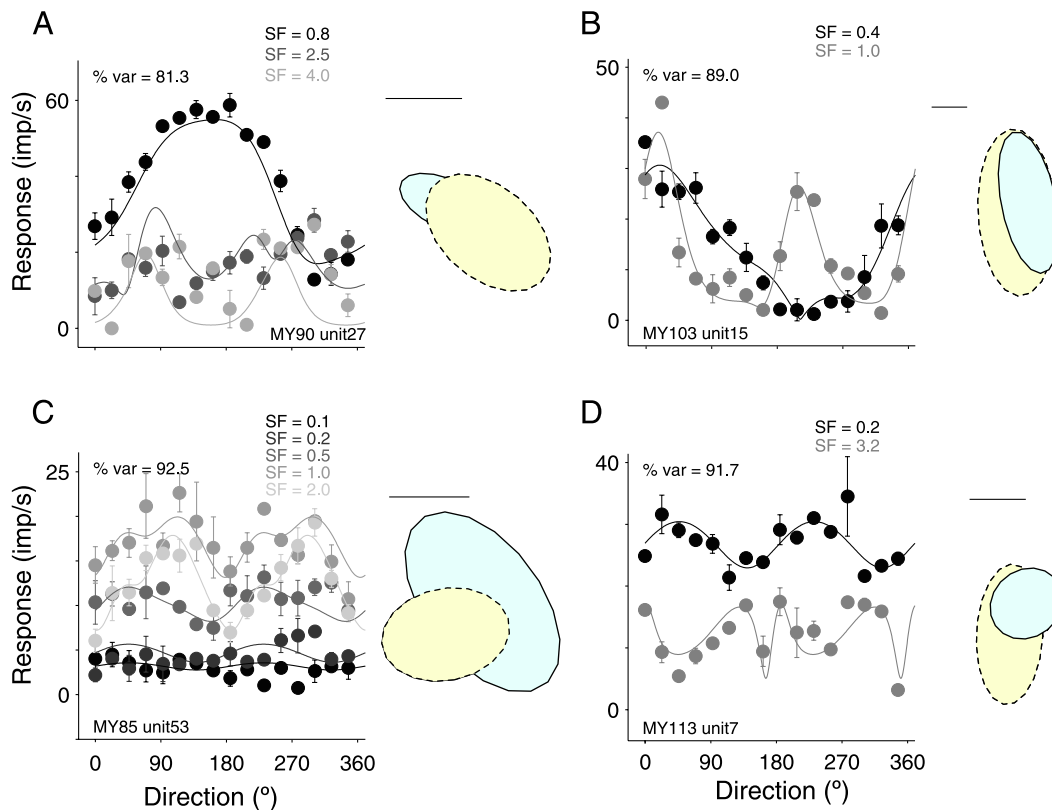


Figure 5. Fits of a linear receptive field model to achromatic direction tuning data obtained from blue-on cells in marmoset LGN at fixed temporal frequency but variable spatial frequency. (A–D) Each panel shows raw responses (filled symbols; error bars show standard errors of the mean, in some cases smaller than the data symbol) and model fits (smooth lines) to data obtained from a single blue-on cell. Responses obtained at different spatial frequencies, and their corresponding model predicted tuning curves, are indicated by the grayscale legends. Inset sketches follow convention as in Figure 4.

Figure 4 also reveals that the achromatic spatial frequency tuning curves of marmoset blue-on cells are not always unimodal—in some instances, there is evidence of two peaks, as in Figure 4F. Such behavior cannot emerge from the standard concentric DOG model. It does however emerge from the elaborated DOG model used here, if spatial frequency tuning is measured along an axis where the On and Off subfields are not arranged concentrically.

Figures 4G and 4H show the results for sample PC and MC cells, obtained by fitting the full model to achromatic direction and spatial frequency tuning data. This illustrates that the model is applicable to the center-surround arrangement of these standard cell types, as shown previously for X-cells in cat retina and LGN (Dawis, Shapley, Kaplan, & Tranchina, 1984), and emphasizes the fundamentally distinct receptive field structure of blue-on cells compared to PC and MC cells.

For the 39 blue-on cells that were tested, the model accounted for a median 93.3% of the variance in responses ($SD = 6.0\%$), and only one cell had less than 80% of response variance accounted for by the model. The best-fit latency of the Off subfield was, on average, 6.3 ms ($SD = 5.2$ ms) longer than that of the On subfield. The correlation between the DI obtained from the raw responses in the

achromatic direction tuning data and the DI obtained for the model predicted responses was 0.94, and the mean angular separation between the vector sum mean direction of the raw and predicted responses was 0.6° . These figures indicate that the model reliably replicates the direction tuning present in the raw responses.

The reader should note that there is a discrepancy between the anatomical predictions and model fits, as follows. The equivalent circle radius of the Off (ML cone dominated) subfield for the model fits was, on average, 1.16 times larger ($SD = 0.54$) than that of the On (S cone dominated) subfield. This result is consistent with our previous analysis of these data using the standard difference-of-Gaussians model (Tailby, Szmajda et al., 2008) and with results from macaque retina (Field et al., 2007; Solomon, Lee, White, Rüttiger, & Martin, 2005; but see also Crook et al., 2009). By contrast, the anatomical results presented in Figure 1 and elsewhere (Dacey, 1993; Ghosh et al., 1997; Rodieck & Watanabe, 1993; Szmajda et al., 2008) show that the outer tier of SBS cells (presumed ML cone recipient) is smaller than the inner (presumed S cone recipient) tier. The relevance of this discrepancy is explored in a later section (see Quantitative comparison of anatomical and physiological results section).

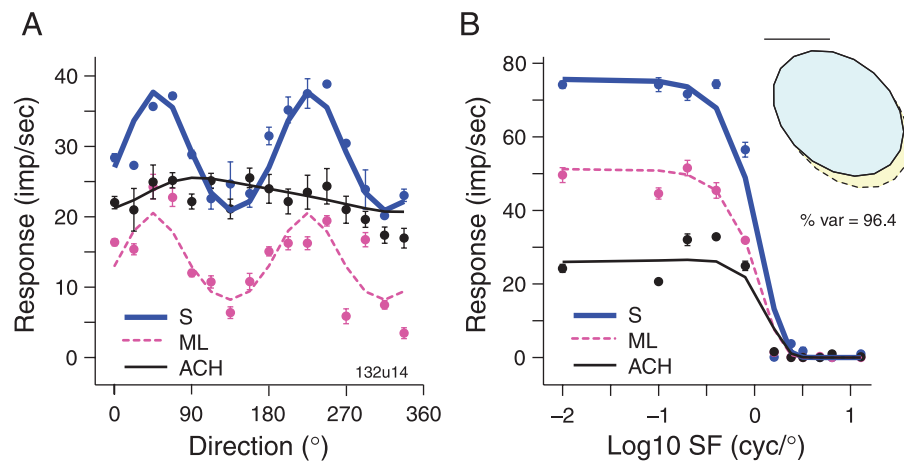


Figure 6. Fits of a linear receptive field model to (A) achromatic (black lines and symbols), ML-cone-isolating (magenta lines and symbols), and S-cone-isolating (blue lines and symbols) direction tuning and (B) spatial frequency tuning data obtained from a blue-on cell in marmoset LGN. All curves were obtained at a single temporal frequency. The inset receptive field sketch in (B) follows convention as in Figure 4. Parameters of the model fit are: On sensitivity = 424.73, On minor axis radius = 0.20 degrees, On major axis radius = 0.28 degrees, On major axis angle = 48.6 degrees, Off sensitivity = -279.82, Off minor axis radius = 0.20 degrees, Off major axis radius = 0.29 degrees, Off major axis angle = 44.8 degrees, Off-x-offset = 0.02 degrees, Off-y-offset = 0.03 degrees, Off relative latency = 4.5 ms.

To provide a second test for the model, we fit achromatic direction tuning curves measured at two or more spatial frequencies. We tested 24 blue-on cells in this way (12 at two spatial frequencies [SFs], 10 at three SFs, 1 at four SFs, 1 at five SFs). For each cell, a single set of parameters was fit simultaneously to direction and spatial frequency data. The model fits were satisfactory: median percentage of variance explained was 82.0%. Fits for four sample cells are shown in Figure 5 (the cell in Figure 5A is also shown in Figure 4F).

For a small number of cells ($n = 3$), we measured direction and spatial frequency tuning for ML-cone-selective gratings as well as for S-cone-selective and achromatic gratings. Parameters were fit simultaneously to all directions, spatial frequencies, and color directions presented. Across the three cells the mean percentage of variance explained was 93.7% ($SD = 4.7\%$). Fits for one sample cell are shown in Figure 6. Using 11 parameters, the model accounts for 96.4% of the variation within the 81 data points. Note that the spatial frequency tuning curve of this cell is low pass for both S-cone-isolating and ML-cone-isolating stimuli, making it an ideal candidate for fitting the model. These data are consistent with our analysis based on achromatic and S-cone-selective gratings and further suggest that a simple linear model based on spatial and temporal asymmetries can account for the direction biases observed in LGN blue-on cells.

Quantitative comparison of anatomical and physiological results

In order to compare quantitatively the physiological data with the anatomical data, in Figure 7 we plot the inferred

receptive field parameters derived from the model fits in the same space as used in Figure 1B. Figure 7A reproduces the data in Figure 1B along with the receptive field properties inferred from the model fits to the data (examples of the model fits are shown in Figure 4). These anatomical and physiological distributions are summarized in Figure 7B by the shaded regions, which define convex hulls (blue: anatomy; red: physiology) including the majority of data points (the vertices of a convex hull enclosing each data set were regarded as outliers). The overlay grid of receptive field caricatures shows sample receptive field arrangements centered on the positions they would plot to in the space. Figure 7B suggests that the spatial offset of the On and Off subfields inferred from the model correspond closely to that implied anatomically. The size of the Off subfield relative to the On subfield, however, differs considerably between the anatomical data and the physiological data: the physiological data suggest that they are comparable in size, whereas the anatomical data suggest that the On (inner tier) region is consistently larger than the Off (outer tier) region. These observations are summarized quantitatively in Figure 7C, which shows marginal histograms for the anatomical (blue outlined bars) and physiological (red shaded bars) data shown in Figure 7A. There is considerable overlap in the histograms of spatial offset, with the geometric mean offset of the physiological distribution being slightly less than that in the anatomical distribution (anatomical: geometric mean = 30.3, $SD = 19.2$; physiological: geometric mean = 19.9, $SD = 31.4$). There is, however, little overlap in the histograms of relative inner/outer radius, the ratio being considerably lower for the anatomical measurements (anatomical: median = 2.1, $SD = 0.85$; physiological: median = 0.96, $SD = 0.5$).

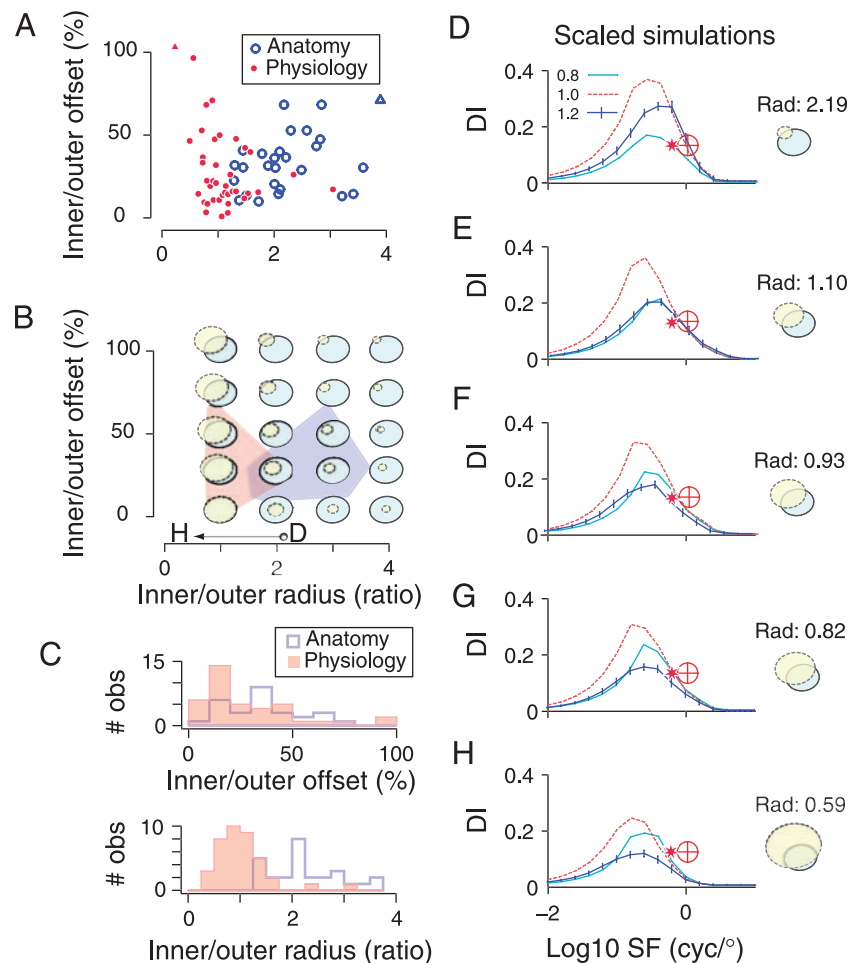


Figure 7. Comparisons of receptive field properties derived anatomically and physiologically. (A) Anatomical data reproduced from Figure 1B; physiological data are from the model fits to the 39 cells described in the text accompanying Figure 4. (B) Each receptive field caricature shows an example of a receptive field morphology that would correspond to a data point centered at that position in the parameter space defined by the x - and y -axes. Shaded regions show the region of the space occupied by the majority of data points (red: physiological; blue: anatomical) from (A). Outliers were removed by disregarding the vertices of a convex hull around the entire data set. (C) Marginal histograms for the data shown in (A). (D–H) DI as a function of spatial frequency. Each panel shows, for three different ratios of [On volume]/[Off volume], the average spatial frequency-dependent DI curves calculated from simulations based on the dendritic field profiles of the 28 SBS cells shown in Figure 1B. The panels differ in the scale factor applied to the spatial profile of the outer tier of the dendritic field (presumed Off). In (D), this scale factor corresponds to that defined anatomically (equivalent area circle radius ratio [On/Off] = 2.19). The magnitude of the scale factor increases in (E) through (H), yielding the On/Off equivalent area circle radius ratios listed above the receptive field caricatures. Note that in the simulations, the scale factor changes the relative area of the Off subfield, but the relative center positions of the On and Off subfields remain unchanged. The red symbols in each panel show the median DI obtained in our sample of recordings from LGN blue-on cells, positioned at the geometric mean spatial frequency used for physiological measurements (red crosshair symbol) or at the spatial frequency appropriate for the anatomical sample (red star symbol). Error bars in D–H show standard deviations.

In the right column of Figure 7, we demonstrate how the spatial frequency dependence of the DI is predicted to vary as a function of the relative radius and volume of the On and Off subfields in the model. The simulations in Figure 7D correspond to the mean anatomical data shown in Figure 1 (across the sample of reconstructed cells, this corresponds to an On/Off equivalent circle radius ratio of 2.19). In Figures 7E–7H, the Off subfield is uniformly “stretched” to give one of four ratio values (1.10, 0.93, 0.82, and 0.59). These values span the range measured in the physiological

recordings. Conceptually, this operation corresponds to leftward translation of the anatomical data in the parameter space used for Figures 7A–7C (solid arrow, Figure 7C). Simulations for three different values of On/Off volume (1.2, 1.0, and 0.8) are shown as separate lines in Figures 7D–7H. In all simulations, relative latency was held fixed at 7 ms.

The simulations predict that despite large variance in the relative size of On and Off subfields, DI is band-pass as a function of spatial frequency, with peak DIs occurring at

spatial frequencies below 1 cyc/deg. The red crosshair symbols in [Figures 7D–7H](#) show the physiologically measured geometric mean DI (0.131), at the geometric mean spatial frequency across all cells measured (1.08 cyc/deg). There appears to be good correspondence between the anatomical ratio value ([Figure 7D](#)) and the mean physiological measured DI. There is, however, a subtle yet important difference between the two sets of measurements. The mean eccentricity of the cells comprising the anatomical data (22.3° , $SD = 15.0^\circ$) is larger than the mean eccentricity of measured receptive fields (4.8° , $SD = 4.9^\circ$). Dendritic and receptive fields increase with increasing eccentricity. Thus, while we have used crosshairs in [Figures 7D–7H](#) to indicate the typical spatial frequency and DI in our physiological sample, the appropriate comparison for the anatomical simulations would be at a greater eccentricity. On the basis of eccentricity-dependent scaling for receptive field size presented by White et al. (2001, their Figure 3), the appropriate SF at the eccentricity of the anatomical measurements is 0.62 cyc/deg. This value is marked by star symbols in [Figures 7D–7H](#). Thus, our physiological data are most consistent with the simulations shown in [Figures 7E](#) and [7F](#), indicating that manipulation of a single parameter (the size of the Off subfield) can bring the anatomical and physiological data into close correspondence.

In summary, while the receptive field model presented here provides a useful conceptual bridge to understanding direction selectivity in blue-on cells, the dimensions of the On and Off subfields cannot simply be equated with the inner and outer tiers of small bistratified cells—spatial pooling of ML cone inputs in blue-on cells must be greater than that implied by the dendritic arbor of the outer tier of small bistratified cells. We return to this point in the [Discussion](#) section.

Discussion

Applicability of the receptive field model

We have applied a receptive field model, which one ideally would evaluate against an extensive range of spatial frequencies and chromaticity. The model does not consider complexities such as the relative sign of M and L cone inputs to blue-on cells in trichromatic retinas (Solomon & Lennie, 2007; Tailby, Solomon et al., 2008), or spatial antagonism between S cones (Tailby, Solomon et al., 2008; Tailby, Szmajda et al., 2008). The model nevertheless reveals how direction selectivity in blue-on cells can arise. The same model (but not the same anatomical substrate) could be applied to studying orientation and direction bias reported for other cell classes of the primate subcortical visual pathway (Passaglia et al., 2002; Smith et al., 1990; Xu et al., 2002).

In recordings from macaque LGN, Wiesel and Hubel (1966) described most “blue” cells as showing Type II receptive field arrangement, that is, where antagonistic RF mechanisms are concentric and of the same size. Subsequent studies, in retina and LGN, have emphasized that many blue-on and blue-off cells do not show Type II organization (Field et al., 2007; Tailby, Solomon et al., 2008; Tailby, Szmajda et al., 2008; but see also Crook et al., 2009; Packer, Verweij, Li, Schnapf, & Dacey, 2010). Our empirical and modeling findings are implicit in the results of Field et al. (2007), who reported spatial and temporal asymmetries between the S-On and ML-Off subfields of blue-on retinal ganglion cells recorded in vitro. Many of their reconstructed receptive field profiles (see their Figure 2) resemble the receptive field subfields recovered by our modeling ([Figure 4](#)). Despite these departures from the canonical Type II arrangement, all these studies nevertheless confirm that the antagonistic On and Off subfields of blue-on cells are much closer in size than are the antagonistic center and surround subfields of PC and MC cells. The direction biases we have explored here are driven by the relative latencies and spatial offset of the subfields, which are of similar (but not necessarily identical) spatial scale.

Our morphological analysis of SBS cells in marmoset retina showed that the inner (presumed On) tier of the dendritic tree is consistently larger than that of the outer (presumed Off) tier ([Figure 1](#), see also Dacey, 1993; Ghosh et al., 1997; Percival et al., 2009; Silveira et al., 1999). The model fits to our direction tuning data obtained from LGN recordings, however, indicate substantial variability, with the Off subfield of the receptive field often larger than the On subfield ([Figures 4, 5, and 7](#)). Compatible findings were reported for in vitro recordings from macaque retina (Field et al., 2007) and in vivo recordings from macaque retina (Solomon et al., 2005; but see also Crook et al., 2009) and marmoset LGN (Tailby, Szmajda et al., 2008). Possible explanations for this discrepancy are convergence of ML cone inputs (via bipolar or amacrine cells) onto the outer tier of the SBS dendritic arbor (Percival et al., 2009), chromatic antagonism at the level of S cone photoreceptors via horizontal cell feedback onto cones (Packer et al., 2010), or convergence of inputs onto blue-on cells at the level of the LGN. These factors would tend to expand the functional size of ML subfield beyond the boundaries predicted by the dendritic dimensions of the outer tier of SBS cells. For example, in marmosets the diffuse bipolar cell classes likely to contact the SBS outer tier draw input from 10 to 13 cones, so should expand functional input to the outer tier by at least $20\ \mu\text{m}$ beyond the dendritic boundaries (Chan, Martin, Clunas, & Grünert, 2001; Percival et al., 2009). For simplicity, we did not incorporate such additional influences into the receptive field model. In any event, the simulations shown in [Figure 7](#) indicate that the relative offset of On and Off subfields is more important than their relative size for generation of direction selectivity at the spatial and temporal frequencies we measured.

The latency of the Off subfield relative to the On subfield observed by Field et al. (2007); ~ 18 ms) is longer than that inferred here (~ 7 ms), which is closer to that reported by Crook et al. (2009). Other work (Yeh, Lee, & Kremers, 1995) is consistent with even smaller latency differences; we have no explanation for these discrepancies.

It is recognized that in constructing receptive fields from L and M cones, there is a trade-off between chromatic and spatial selectivities (DeValois & DeValois, 1993; Ingling & Martinez, 1985; Lennie & Movshon, 2005), because any given position on the retina can only be occupied by a single photoreceptor. In the same way, chromatic selective circuits feeding S cone signals to SBS cells should produce spatial anisotropy in the receptive field as a result of the wide space between S cones (e.g., Figure 1). We show here that a by-product of these anisotropies is spatiotemporal frequency-dependent direction selectivity for achromatic gratings. As yet we do not know whether convergence in the retina or the LGN (Solomon et al., 2002; Tailby, Szmajda et al., 2008) works to amplify or diminish this direction bias. Direct comparisons of the dendritic field morphology and direction bias of identified SBS cells (Dacey & Lee, 1994; Yeh et al., 1995) are required to verify the model.

Direction selectivity at different stages along the mammalian visual pathway

Direction selectivity in the retino-geniculo-cortical pathway is customarily described as an emergent property of primary visual cortex circuitry (Andersen, 1997; Hubel & Wiesel, 1968). Overtly direction-selective retinal ganglion cells (DSGCs) have been reported in non-primate mammalian retina (rabbit: Barlow, Hill, & Levick, 1964; Barlow & Levick, 1965; Vaney, Levick, & Thibos, 1981; cat: Cleland & Levick, 1974), and Huberman et al. (2009) demonstrated a thalamic projection from On–Off DSGCs in mouse. Our population data (Figure 3) show that in primate LGN, direction biases can be strongly expressed in geniculate neurons that receive S cone input. How do our data relate to the kinds of direction selectivity observed in retina, V1, and beyond?

While it has often been speculated that DSGCs are also present in primate retina, they have not yet been identified. The direction selectivity we observed in S cone recipient cells of marmoset LGN differs in a number of respects from that of DSGCs found in other species. First (although not tested directly), On–Off DSGCs in other species are not considered to receive distinct spectral signatures to On and Off subfields (Vaney & Taylor, 2002). Second (Figures 3L and 3M), we saw no evidence for clustering of preferred directions around particular visual axes (Barlow et al., 1964; Caldwell & Daw, 1978; Huberman et al., 2009; Vaney & Taylor, 2002). Third, blue-on cells gave modulated responses to all directions and we saw little evidence of inhibition from stimuli moving in the non-preferred

direction. Responses of 25% (11/49) of blue-on cells were suppressed (by at least 2 SEM relative to maintained discharge) on presentation of anti-preferred gratings, and on average the ratio of the evoked to maintained discharge for the non-preferred direction was 1.4 (geometric mean; $SD = 4.8$). Finally, the direction selectivity we observed in blue-on cells is highly dependent on stimulus parameters, whereas that of DSGCs is relatively stimulus invariant (Grzywacz & Amthor, 2007). For these reasons, we believe that our recordings are not related to the DSGCs described so far in the above-mentioned studies.

Xu et al. (2002) reported responses to drifting gratings in LGN of the nocturnal monkey *Aotus* and found approximately 19% of encountered cells showed DI above a criterion value of 0.08, with little difference between parvocellular, magnocellular, and koniocellular neurons. Their result is likely compatible with ours when two facts are taken into account. First, the criterion value used by these authors is slightly less stringent than the criterion DI (0.1) used in the present study. Second, the *Aotus* shows monochromatic cone vision lacking S cones (Jacobs, Deegan, Neitz, Crognale, & Neitz, 1993; Levenson, Fernandez-Duque, Evans, & Jacobs, 2007). Consistently, there are no reports of cells showing blue-on response properties in recordings from *Aotus* (Kilavik, Silveira, & Kremers, 2007; Silveira et al., 2004; Usrey & Reid, 2000; Xu et al., 2002).

In recordings from cat primary visual cortex, Hubel and Wiesel (1962) described a subset of units that responded to movement of a slit of light in one direction, but not when it was moved in the opposite direction. Such cortical neurons are appropriately described as direction selective because they are inhibited by motion in the anti-preferred direction (Hammond & Pomfrett, 1989; Henry, Bishop, & Dreher, 1974; Movshon & Newsome, 1996). Further, their spatial frequency tuning is normally band-pass (DeValois, Albrecht, & Thorell, 1982; Hawken, Parker, & Lund, 1988), and their direction preference is robust to variation in spatial and temporal frequencies (Hammond & Pomfrett, 1989; McLean & Palmer, 1994). By contrast, blue-on cells do respond (albeit at lower amplitude) to anti-preferred image drift direction and exhibit direction biases that are sensitive to changes in spatial frequency (Figures 3C, 3E, and 5).

Direction selectivity is a conspicuous property of the majority of neurons in area MT, and this area receives a direct projection from the koniocellular layers (Benevento & Yoshida, 1981; Sincich, Park, Wohlgenuth, & Horton, 2004; Warner, Goldshmit, & Bourne, 2010; Yukie & Iwai, 1981). Could a projection from direction-selective blue-on cells contribute to direction selectivity in area MT? We believe this possibility, although intriguing, is unlikely. The instability of direction selectivity observed in our sample of blue-on cells argues against their responses being useful in the decoding of stimulus motion. Further, although the dominant functional input to blue-on cells comes from S cones, the contribution of S cones to responses in MT neurons is

unlikely to be more than expected by random cone connections (Riecansky, Thiele, Distler, & Hoffmann, 2005). Finally, if MT neurons show direction selectivity for S-cone-selective stimuli (Seidemann, Poirson, Wandell, & Newsome, 1999; but see also Riecansky et al., 2005), then that signal is likely to be developed within MT rather than inherited from a blue-on input stream, because we observe negligible direction biases when blue-on cells are stimulated with S-cone-selective gratings.

Conclusion

Diversity of functional properties observed in blue-on cells implies substantial variation in receptive field structure. Adequate characterization of S cone recipient neurons in retina or LGN thus needs to take account of this fact. The receptive field model presented here is flexible enough to account for the observed functional heterogeneity.

Acknowledgments

We thank D. Matin, P. Jusuf, and B. Eriköz for histological analysis, A. Lara for technical assistance, and P. Bedggood for the ZEMAX predictions. This study was supported by the Australian National Health and Medical Research Council Grant 566558, the Australian Research Council Grant 0984649, and the Victorian Lions Foundation. Author BAS was supported by a University of Melbourne graduate study scholarship.

Commercial relationships: none.

Corresponding author: Paul R. Martin.

Email: prmartin@sydney.edu.au.

Address: Discipline of Clinical Ophthalmology and Save Sight Institute, University of Sydney, Eye Hospital Campus, Macquarie St., GPO Box 4337, Sydney NSW 2001, Australia.

References

- Andersen, R. A. (1997). Neural mechanisms of visual motion perception in primates. *Neuron*, *18*, 865–872.
- Barlow, H. B., Hill, R. M., & Levick, W. R. (1964). Retinal ganglion cells responding selectively to direction of movement in ganglion cells of the rabbit retina. *The Journal of Physiology*, *178*, 477–504.
- Barlow, H. B., & Levick, W. R. (1965). The mechanism of directionally selective units in rabbit's retina. *The Journal of Physiology*, *178*, 477–504.
- Benevento, L. A., & Yoshida, K. (1981). The afferent and efferent organization of the lateral geniculo-prestriate pathways in the macaque monkey. *Journal of Comparative Neurology*, *203*, 455–474.
- Blessing, E. M., Solomon, S. G., Hashemi-Nezhad, M., Morris, B. J., & Martin, P. R. (2004). Chromatic and spatial properties of parvocellular cells in the lateral geniculate nucleus of the marmoset (*Callithrix jacchus*). *The Journal of Physiology*, *557*, 229–245.
- Brainard, D. H. (1996). Cone contrast and opponent modulation color spaces. In P. K. Kaiser & G. M. Boynton (Eds.), *Human color vision* (pp. 563–577). Washington, DC: Optical Society of America.
- Caldwell, J. H., & Daw, N. W. (1978). New properties of rabbit retinal ganglion cells. *The Journal of Physiology*, *276*, 257–276.
- Calkins, D. J., Tsukamoto, Y., & Sterling, P. (1998). Microcircuitry and mosaic of a blue–yellow ganglion cell in the primate retina. *Journal of Neuroscience*, *18*, 3373–3385.
- Chan, T. L., Martin, P. R., Clunas, N., & Grünert, U. (2001). Bipolar cell diversity in the primate retina: Morphologic and immunocytochemical analysis of a New World monkey, the marmoset *Callithrix jacchus*. *Journal of Comparative Neurology*, *437*, 219–239.
- Chichilnisky, E. J., & Baylor, D. A. (1999). Receptive-field microstructure of blue–yellow ganglion cells in primate retina. *Nature Neuroscience*, *2*, 889–893.
- Cleland, B. G., & Levick, W. R. (1974). Properties of rarely encountered types of ganglion cells in the cat's retina and an overall classification. *The Journal of Physiology*, *240*, 457–492.
- Crook, J. D., Davenport, C. M., Peterson, B. B., Packer, O. S., Detwiler, P. B., & Dacey, D. M. (2009). Parallel ON and OFF cone bipolar inputs establish spatially coextensive receptive field structure of blue–yellow ganglion cells in primate retina. *Journal of Neuroscience*, *29*, 8372–8387.
- Dacey, D. M. (1993). Morphology of a small-field bistratified ganglion cell type in the macaque and human retina. *Visual Neuroscience*, *10*, 1081–1098.
- Dacey, D. M., & Lee, B. B. (1994). The “blue-on” opponent pathway in primate retina originates from a distinct bistratified ganglion cell type. *Nature*, *367*, 731–735.
- Dawis, S., Shapley, R., Kaplan, E., & Tranchina, D. (1984). The receptive field organization of X-cells in the cat: Spatiotemporal coupling and asymmetry. *Vision Research*, *24*, 549–564.
- DeMonasterio, F. M., & Gouras, P. (1975). Functional properties of ganglion cells of the rhesus monkey retina. *The Journal of Physiology*, *251*, 167–195.

- Derrington, A. M., Krauskopf, J., & Lennie, P. (1984). Chromatic mechanisms in lateral geniculate nucleus of macaque. *The Journal of Physiology*, *357*, 241–265.
- DeValois, R. L., Abramov, I., & Jacobs, G. H. (1966). Analysis of response patterns of LGN cells. *Journal of the Optical Society of America*, *56*, 966–977.
- DeValois, R. L., Albrecht, D. G., & Thorell, L. G. (1982). Spatial frequency selectivity of cells in macaque visual cortex. *Vision Research*, *22*, 545–559.
- DeValois, R. L., & DeValois, K. K. (1993). A multi-stage color model. *Vision Research*, *33*, 1053–1065.
- Dreher, B., Fukada, Y., & Rodieck, R. W. (1976). Identification, classification and anatomical segregation of cells with X-like and Y-like properties in the lateral geniculate nucleus of Old-World primates. *The Journal of Physiology*, *258*, 433–452.
- Enroth-Cugell, C., & Robson, J. (1966). The contrast sensitivity of retinal ganglion cells of the cat. *The Journal of Physiology*, *187*, 517–552.
- Field, G. D., Sher, A., Gauthier, J. L., Greschner, M., Shlens, J., Litke, A. M., et al. (2007). Spatial properties and functional organization of small bistratified ganglion cells in primate retina. *Journal of Neuroscience*, *27*, 13261–13272.
- Forte, J. D., Hashemi-Nezhad, M., Dobbie, W. J., Dreher, B., & Martin, P. R. (2005). Spatial coding and response redundancy in parallel visual pathways of the marmoset *Callithrix jacchus*. *Visual Neuroscience*, *22*, 479–491.
- Ghosh, K. K., & Grünert, U. (1999). Synaptic input to small bistratified (blue-on) ganglion cells in the retina of a New World monkey, the marmoset *Callithrix jacchus*. *Journal of Comparative Neurology*, *413*, 417–428.
- Ghosh, K. K., Martin, P. R., & Grünert, U. (1997). Morphological analysis of the blue cone pathway in the retina of a New World monkey, the marmoset *Callithrix jacchus*. *Journal of Comparative Neurology*, *379*, 211–225.
- Grzywacz, N. M., & Amthor, F. R. (2007). Robust directional computation in on–off directionally selective ganglion cells of rabbit retina. *Visual Neuroscience*, *24*, 647–661.
- Hammond, P., & Pomfrett, C. J. (1989). Directional and orientational tuning of feline striate cortical neurones: Correlation with neuronal class. *Vision Research*, *29*, 653–662.
- Hawken, M. J., Parker, A. J., & Lund, J. S. (1988). Laminar organization and contrast sensitivity of direction-selective cells in the striate cortex of the Old World monkey. *Journal of Neuroscience*, *8*, 3541–3548.
- Hendry, S. H. C., & Reid, R. C. (2000). The koniocellular pathway in primate vision. *Annual Review of Neuroscience*, *23*, 127–153.
- Henry, G. H., Bishop, P. O., & Dreher, B. (1974). Orientation, axis and direction as stimulus parameters for striate cells. *Vision Research*, *14*, 767–777.
- Hubel, D. H., & Wiesel, T. N. (1962). Receptive fields, binocular interaction and functional architecture in the cat's visual cortex. *The Journal of Physiology*, *160*, 106–154.
- Hubel, D. H., & Wiesel, T. N. (1968). Receptive fields and functional architecture of monkey striate cortex. *The Journal of Physiology*, *195*, 215–243.
- Huberman, A. D., Wei, W., Elstrott, J., Stafford, B. K., Feller, M. B., & Barres, B. A. (2009). Genetic identification of an On–Off direction-selective retinal ganglion cell subtype reveals a layer-specific subcortical map of posterior motion. *Neuron*, *62*, 327–334.
- Ingling, C. R., & Martinez, E. (1985). The spatio-temporal properties of the r–g cell channel. *Vision Research*, *18*, 379–390.
- Jacobs, G. H., Deegan, J. F., II, Neitz, J., Crognale, M. A., & Neitz, M. (1993). Photopigments and color vision in the nocturnal monkey, *Aotus*. *Vision Research*, *33*, 1773–1783.
- Kilavik, B. E., Silveira, L. C., & Kremers, J. (2007). Spatial receptive field properties of lateral geniculate cells in the owl monkey (*Aotus azarae*) at different contrasts: A comparative study. *European Journal of Neuroscience*, *26*, 992–1006.
- Lee, B. B., Valberg, A., Tigwell, D. A., & Tryti, J. (1987). An account of responses of spectrally opponent neurons in macaque lateral geniculate nucleus to successive contrast. *Proceedings of the Royal Society of London B*, *230*, 293–314.
- Lennie, P., & Movshon, J. A. (2005). Coding of color and form in the geniculostriate visual pathway. *Journal of the Optical Society of America*, *22*, 2013–2033.
- Levenson, D. H., Fernandez-Duque, E., Evans, S., & Jacobs, G. H. (2007). Mutational changes in S-cone opsin genes common to both nocturnal and cathemeral *Aotus* monkeys. *American Journal of Primatology*, *69*, 757–765.
- Levick, W. R., & Thibos, L. N. (1982). Analysis of orientation bias in cat retina. *The Journal of Physiology*, *329*, 243–261.
- Marshak, D., Stafford, D., Jacoby, R., & Kouyama, N. (1995). Blue cone bipolar cells of the macaque retina. In B. Drum (Ed.), *Colour vision deficiencies XII. Twelfth symposium of the international research group on colour vision deficiencies* (pp. 277–283). Tübingen, Germany: Kluwer Academic Publishers.

- Martin, P. R., & Grünert, U. (1999). Analysis of the short wavelength sensitive (“blue”) cone mosaic in the primate retina: A comparison of New World and Old World monkeys. *Journal of Comparative Neurology*, *406*, 1–14.
- Martin, P. R., Grünert, U., Chan, T. L., & Bumsted, K. (2000). Spatial order in short-wavelength-sensitive cone photoreceptors: A comparative study of the primate retina. *Journal of the Optical Society of America*, *17*, 557–567.
- Martin, P. R., White, A. J. R., Goodchild, A. K., Wilder, H. D., & Sefton, A. E. (1997). Evidence that blue-on cells are part of the third geniculocortical pathway in primates. *European Journal of Neuroscience*, *9*, 1536–1541.
- McLean, J., & Palmer, L. A. (1994). Organization of simple cell responses in the three-dimensional (3-D) frequency domain. *Visual Neuroscience*, *11*, 295–306.
- Movshon, J. A., & Newsome, W. T. (1996). Visual response properties of striate cortical neurons projecting to area MT in macaque monkeys. *Journal of Neuroscience*, *16*, 7733–7741.
- Packer, O. S., Verweij, J., Li, P. H., Schnapf, J. L., & Dacey, D. M. (2010). Blue–yellow opponency in primate S cone photoreceptors. *Journal of Neuroscience*, *30*, 568–572.
- Passaglia, C. L., Troy, J. B., Rüttiger, L., & Lee, B. B. (2002). Orientation sensitivity of ganglion cells in primate retina. *Vision Research*, *42*, 683–694.
- Percival, K. A., Jusuf, P. R., Martin, P. R., & Grünert, U. (2009). Synaptic inputs onto small bistratified (blue-ON/yellow-OFF) ganglion cells in marmoset retina. *Journal of Comparative Neurology*, *517*, 655–669.
- Rieicansky, I., Thiele, A., Distler, C., & Hoffmann, K. P. (2005). Chromatic sensitivity of neurones in area MT of the anaesthetised macaque monkey compared to human motion perception. *Experimental Brain Research*, *167*, 504–525.
- Rodieck, R. W., & Stone, J. (1965). Analysis of receptive fields of cat retinal ganglion cells. *Journal of Neurophysiology*, *28*, 833–849.
- Rodieck, R. W., & Watanabe, M. (1993). Survey of the morphology of macaque retinal ganglion cells that project to the pretectum, superior colliculus, and parvocellular laminae of the lateral geniculate nucleus. *Journal of Comparative Neurology*, *338*, 289–303.
- Roy, S., Martin, P. R., Dreher, B., Saalman, Y. B., Hu, D., & Vidyasagar, T. R. (2009). Segregation of short-wavelength sensitive (S) cone signals in the macaque dorsal lateral geniculate nucleus. *European Journal of Neuroscience*, *30*, 1517–1526.
- Seidemann, E., Poirson, A. B., Wandell, B. A., & Newsome, W. T. (1999). Color signals in area MT of the macaque monkey. *Neuron*, *24*, 911–917.
- Silveira, L. C., Saito, C. A., Lee, B. B., Kremers, J., daSilvaFilho, M., Kilavik, B. E., et al. (2004). Morphology and physiology of primate M- and P-cells. *Progress in Brain Research*, *144*, 21–46.
- Silveira, L. C. L., Lee, B. B., Yamada, E. S., Kremers, J., Hunt, D. M., Martin, P. R., et al. (1999). Ganglion cells of a short wavelength sensitive cone pathway in New World monkeys: Morphology and physiology. *Visual Neuroscience*, *16*, 333–343.
- Sincich, L. C., Park, K. F., Wohlgemuth, M. J., & Horton, J. C. (2004). Bypassing V1: A direct geniculate input to area MT. *Nature Neuroscience*, *7*, 1123–1128.
- Smith, E. L., Chino, Y. M., Ridder, W. H., Kitagawa, K., & Langston, A. (1990). Orientation bias of neurons in the lateral geniculate nucleus of macaque monkeys. *Visual Neuroscience*, *5*, 525–545.
- Solomon, S. G., Lee, B. B., White, A. J., Rüttiger, L., & Martin, P. R. (2005). Chromatic organization of ganglion cell receptive fields in the peripheral retina. *Journal of Neuroscience*, *25*, 4527–4539.
- Solomon, S. G., & Lennie, P. (2007). The machinery of colour vision. *Nature Reviews Neuroscience*, *8*, 276–286.
- Solomon, S. G., White, A. J. R., & Martin, P. R. (2002). Extra-classical receptive field properties of parvocellular, magnocellular and koniocellular cells in the primate lateral geniculate nucleus. *Journal of Neuroscience*, *22*, 338–349.
- Soodak, R. E. (1986). Two-dimensional modeling of visual receptive fields using Gaussian subunits. *Proceedings of the National Academy of Sciences of the United States of America*, *83*, 9259–9263.
- Szmajda, B. A., Martin, P. R., & Grünert, U. (2008). Retinal ganglion cell inputs to the koniocellular pathway. *Journal of Comparative Neurology*, *510*, 251–268.
- Tailby, C., Solomon, S. G., & Lennie, P. (2008). Functional asymmetries in visual pathways carrying S-cone signals in macaque. *Journal of Neuroscience*, *28*, 4078–4087.
- Tailby, C., Szmajda, B. A., Buzás, P., Lee, B. B., & Martin, P. R. (2008). Transmission of blue (S) cone signals through the primate lateral geniculate nucleus. *The Journal of Physiology*, *585*, 5947–5967.
- Troilo, D., Howland, H. C., & Judge, S. J. (1993). Visual optics and retinal cone topography in the common marmoset (*Callithrix jacchus*). *Vision Research*, *33*, 1301–1310.

- Usrey, W. M., & Reid, R. C. (2000). Visual physiology of the lateral geniculate nucleus in two species of New World monkey: *Saimiri sciureus* and *Aotus trivirgatus*. *The Journal of Physiology*, *523*, 755–769.
- Vaney, D. I., Levick, W. R., & Thibos, L. N. (1981). Rabbit retinal ganglion cells: Receptive field classification and axonal conduction properties. *Experimental Brain Research*, *44*, 27–33.
- Vaney, D. I., & Taylor, W. R. (2002). Direction selectivity in the retina. *Current Opinion in Neurobiology*, *12*, 405–410.
- Victor, J. D., Blessing, E. M., Forte, J., Buzás, P., & Martin, P. R. (2007). Response variability of marmoset parvocellular neurons. *The Journal of Physiology*, *579*, 29–51.
- Warner, C. E., Goldshmit, Y., & Bourne, J. A. (2010). Retinal afferents synapse with relay cells targeting the middle temporal area in the pulvinar and lateral geniculate nuclei. *Frontiers in Neuroanatomy*, *4*, 8/1–8/16.
- White, A. J. R., Solomon, S. G., & Martin, P. R. (2001). Spatial properties of koniocellular cells in the lateral geniculate nucleus of the marmoset *Callithrix jacchus*. *The Journal of Physiology*, *533*, 519–535.
- Wiesel, T. N., & Hubel, D. (1966). Spatial and chromatic interactions in the lateral geniculate body of the rhesus monkey. *Journal of Neurophysiology*, *29*, 1115–1156.
- Williams, D. R., & Hofer, H. (2003). Formation and acquisition of the retinal image. In L. M. Chalupa & J. S. Werner (Eds.), *The visual neurosciences* (pp. 795–810). Cambridge, MA: The MIT press.
- Xu, X., Ichida, J., Shostak, Y., Bonds, A. B., & Casagrande, V. A. (2002). Are primate lateral geniculate nucleus (LGN) cells really sensitive to orientation or direction? *Visual Neuroscience*, *19*, 97–108.
- Yamada, E. S., Silveira, L. C. L., Gomes, F. L., & Lee, B. B. (1996). The retinal ganglion cell classes of New World primates. *Revista Brasileira de Biologia*, *56*, 381–396.
- Yeh, T., Lee, B. B., & Kremers, J. (1995). Temporal response of ganglion cells of the macaque retina to cone-specific modulation. *Journal of the Optical Society of America A*, *12*, 456–464.
- Yukie, M., & Iwai, E. (1981). Direct projection from the dorsal lateral geniculate nucleus to the prestriate cortex in macaque monkeys. *Journal of Comparative Neurology*, *201*, 81–97.